Crystalline electric field of the rare-earth nickelates $R\mathrm{NiO_3}$ (R=Pr, Nd, Sm, Eu, and $\mathrm{Pr_{1-x}La_x}$, $0 \leqslant x \leqslant 0.7$) determined by inelastic neutron scattering

S. Rosenkranz,* M. Medarde, F. Fauth, J. Mesot, M. Zolliker, and A. Furrer
Laboratory for Neutron Scattering, ETH Zürich & Paul Scherrer Institute, 5232 Villigen PSI, Switzerland

U. Staub
Swiss Light Source Project, Paul Scherrer Institute, 5232 Villigen PSI, Switzerland

P. Lacorre
Laboratoire des Fluorures, UPRES-A CNRS 6010, Université du Maine, 72085 Le Mans Cedex, France

R. Osborn
Materials Science Divison, Argonne National Laboratory, Argonne, Illinois 60439

R. S. Eccleston
ISIS Facility, Rutherford Appleton Laboratory, Chilton, Didcot OX11 0QX, United Kingdom

V. Trounov
Petersburg Nuclear Physics Institute, 188358 Gatchina, Russia
(Received 29 July 1999)

The rare-earth based nickelates $R\mathrm{NiO_3}$ (R=Pr, Nd, Sm, Eu, and $\mathrm{Pr_{1-x}La_x}$, $0 \leqslant x \leqslant 0.7$) were studied by inelastic neutron scattering. Energy splittings due to the crystalline-electric-field (CEF) interaction at the R^{3+} site within the electronic ground-state J multiplet (for R=Pr, Nd, and $\mathrm{Pr_{1-x}La_x}$) as well as within the two lowest-lying J multiplets (for R=Sm and Eu) were directly observed, and the corresponding CEF energy-level schemes were reconstructed. The latter were rationalized in terms of CEF parameters, which vary smoothly over the rare-earth series and give magnetic properties associated with the R sublattice in agreement with results from neutron powder diffraction experiments. Across the metal-insulator transition, a continuous change in the electronic part of the CEF parameters is observed. However, an attempt to quantify a charge transfer from the observed variation of the CEF parameters in an effective point charge model failed, probably due to the strong covalency in these compounds. Across the structural transition occurring in $\mathrm{Pr_{1-x}La_xNiO_3}$ at $x=0.7$, a change in the symmetry of the CEF ground state is observed, which has a profound influence on the thermodynamic properties. [S0163-1829(99)01145-5]

I. INTRODUCTION

After the discovery of high-temperature superconductivity in copper-oxide perovskites there has been increasing interest in metal-oxide systems exhibiting high electrical conductivity. The nickelates $R\mathrm{NiO_3}$ (R = rare earth) belong to these systems, and they have the outstanding property of displaying metallic conductivity even without doping.[1] Whereas $\mathrm{LaNiO_3}$ remains metallic in the whole temperature range, a sharp metal-insulator (MI) transition has been observed for the nickelates with R=Pr, Nd, Sm, and Eu with transition temperatures T_{MI}= 135, 200, 400, and 480 K, respectively.[2] It was found that T_{MI} depends strongly on both internal (chemical) and external pressure with extraordinarily high values $\partial \mathrm{T_{MI}}/\partial P_{\mathrm{ext}} \approx -8$ K/kbar.[3,4] Neutron-diffraction experiments revealed a linear relation between the metal-insulator transition and the tilting angle of the $\mathrm{NiO_6}$ octahedra.[5,6] For R=Pr and Nd, the MI transition is accompanied by a long-range antiferromagnetic ordering of the Ni sublattice, whereas for R=Sm and Eu, the Néel temperature is much lower than T_{MI} (T_N=223 and 205 K, respectively).[7–9] The phase diagram resulting from resistivity,[2] muon spin relaxation,[7] and neutron-scattering experiments[8–13] of all the rare-earth nickelates studied in the present work is shown in Fig. 1.

The MI transition in the nickelates is believed to be accompanied by a loss of covalency in the Ni-O bonds, i.e., a transfer of electrons from the Ni to the O sites.[5,7] Through studying the crystalline-electric-field (CEF) interaction at the R site, such a charge transfer could possibly be observed as was recently demonstrated for the cuprates $R\mathrm{Ba_2Cu_3O_x}$ ($6 \leqslant x \leqslant 7$) with R=Er (Ref. 14) and Ho (Ref. 15). In order to be able to arrive at such a conclusion, however, a very detailed knowledge of the CEF interaction is required. The CEF interaction is also important to rationalize the observed magnetic moment of the rare-earth ions in $\mathrm{SmNiO_3}$ and $\mathrm{NdNiO_3}$ induced by the R-Ni exchange coupling.[16] Another important aspect is the behavior of the Pr^{3+} CEF ground state across the transition from the orthorhombic to the rhombohedral symmetry in $\mathrm{Pr_{1-x}La_xNiO_3}$ (see Fig. 1). For this transition, a change of the ground-state symmetry from a singlet to a non-Kramers doublet is possible, which would strongly affect the thermodynamic properties. With these considerations in mind, we investigated the CEF interaction

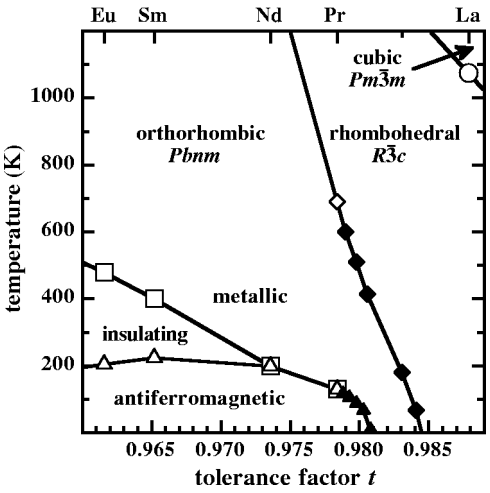

FIG. 1. Phase diagram of rare-earth nickelates $R\mathrm{NiO_3}$ as a function of the tolerance factor $t=d_{\mathrm{R\text{-}O}}/(\sqrt{2}d_{\mathrm{Ni\text{-}O}})$, where $d_{\mathrm{R\text{-}O}}$ and $d_{\mathrm{Ni\text{-}O}}$ denote the average first neighbor *R*-O and Ni-O distance, respectively. The solid symbols denote the solid solutions $\mathrm{Pr_{1-x}La_xNiO_3}$.

of the rare-earth nickelates in detail by the inelastic neutron scattering (INS) technique, the experimental tool of choice for studying optically opaque materials.

The synthesis as well as the structural, magnetic, and electronic properties of the rare-earth nickelates have recently been reviewed in a comprehensive article by Medarde,[16] to which we refer for further details. Here we concentrate on the CEF interaction in these compounds. Section II provides a brief introduction into the INS technique applied to the measurements of CEF splittings. In Sec. II C we summarize the symmetry aspects of the CEF interaction in the rare-earth nickelates. The experimental procedure, the results, and the data analysis are presented in Sec. III. In Sec. IV we discuss our results and give some final conclusions.

II. INELASTIC NEUTRON SCATTERING (INS)

A. Neutron-scattering cross-section

The CEF interaction gives rise to discrete energy levels that can be spectroscopically determined by the INS technique. In the experiment the sample is irradiated by a monochromatic neutron beam, and the scattered neutrons are analyzed according to the energy transfer

$$\hbar\omega=\frac{\hbar^2}{2m}(\mathbf{k}_0^2-\mathbf{k}_1^2), \tag{1}$$

where m denotes the neutron mass, and $\mathbf{k}_0$, $\mathbf{k}_1$ are the wave vectors of incoming and scattered neutrons, respectively. The corresponding momentum transfer is given by

$$\mathbf{Q}=\mathbf{k}_0-\mathbf{k}_1, \tag{2}$$

where $\mathbf{Q}$ is the scattering vector. In these experiments both energy gain and energy loss processes can be measured, i.e., the R^{3+} ion is either excited from a lower to a higher state ($\hbar\omega>0$) and the neutron loses the corresponding energy, or vice versa. Therefore, one expects the measured energy spectrum to exhibit resonance peaks that can be attributed to transitions between different CEF levels. In the analysis of these peaks a unique identification of the observed transitions is only possible by considering the relative intensities of the various transitions. For a system of N noninteracting ions the thermal neutron cross-section for the CEF transition $|i\rangle\rightarrow|j\rangle$ is given in the dipole approximation by[17]

$$\frac{\partial^2\sigma}{\partial\Omega\,\partial\omega}=\frac{N}{Z}\left(\frac{\gamma e^2}{m_e c^2}\right)^2\frac{k_1}{k_0}f^2(Q)e^{-2W}e^{-E_i/k_BT}\times|\langle j|\mathbf{m}_p|i\rangle|^2\delta(E_i-E_j+\hbar\omega), \tag{3}$$

where E_i and E_j are the energies of the CEF states $|i\rangle$ and $|j\rangle$, respectively, W is the Debye-Waller factor, $f(Q)$ the magnetic form factor, and $\mathbf{m}_p$ the component of the magnetic moment operator perpendicular to the scattering vector $\mathbf{Q}$. The remaining symbols have their usual meaning. Some of the transition matrix elements $\langle j|\mathbf{m}_p|i\rangle$ are zero by symmetry, thus leading to strict selection rules for INS transitions.

One problem remains, namely the question whether peaks observed in the energy spectra really arise from CEF transitions or whether they result from other dynamic processes, like phonon scattering. However, CEF transitions may be distinguished from phonon processes by the way in which the intensities vary with temperature and momentum transfer. As can be seen from the cross-section formula (3), the CEF intensity decreases with increasing modulus of the scattering vector $\mathbf{Q}$ according to $f^2(Q)$, whereas the phonon peak intensity usually increases with Q^2 (apart from the modulation due to the structure factor). Furthermore, phonons obey Bose statistics, whereas the population of CEF levels is governed by Boltzmann statistics.

B. Instrumental aspects

The determination of CEF excitations by neutron-scattering techniques requires a controlled access to the variables $\mathbf{Q}$ and ω, which can be done in various ways. A very effective experimental method is triple-axis crystal spectrometry in which an incident beam of neutrons with a well-defined wave vector $\mathbf{k}_0$ is selected from the white spectrum of the neutron source by the monochromator crystal (first axis). The monochromatic neutron beam is then scattered from the sample (second axis). The intensity of the scattered beam with wave vector $\mathbf{k}_1$ is measured by the analyzer crystal (third axis) and the neutron detector, thereby defining the energy transfer $\hbar\omega$ as well. The outstanding advantage of the triple-axis spectrometer is that data can be taken at predetermined points in reciprocal space (which is known as the ''constant-$\mathbf{Q}$'' or ''constant-ω'' method), so that single-crystal measurements of the dispersion relation $\hbar\omega(\mathbf{Q})$ can be performed in a controlled manner. For the present experiments we have used the triple-axis spectrometer MARC at the reactor Saphir of the Paul Scherrer Institute at Villigen (Switzerland) as well as the triple-axis spectrometer IN3 at the high-flux reactor of the Institut Laue-Langevin at Grenoble (France).

For experiments on polycrystalline materials various types of time-of-flight spectrometer are usually more appropriate. In direct time-of-flight spectrometers, the neutron beam is monochromated by a series of choppers, which produce pulses of neutrons with the desired wavelength as well as eliminate higher-order neutrons and prevent frame overlap

of pulses from different repetition periods. The monochromatic neutron pulses are scattered from the sample, and the scattered neutrons are detected by arrays of neutron counters covering a large solid angle. The energy transfer $\hbar\omega$ and the modulus of the scattering vector $\mathbf{Q}$ are then determined by the flight time of the neutron (from the sample to the detector) and the scattering angle (at which the detector is positioned), respectively. For the present experiments we have used the time-of-flight spectrometers HET and MARI at the spallation source ISIS of the Rutherford Appleton Laboratory at Didcot (UK) as well as the time-of-flight spectrometer LRMECS at the spallation source IPNS of the Argonne National Laboratory at Argonne (USA).

C. The crystalline electric field (CEF)

The degeneracy of the free ion J multiplets of a rare-earth ion embedded in a crystal lattice is partly removed by the CEF potential produced by the charge distribution of the surrounding ligand ions. Using tensor operator techniques, the CEF Hamiltonian takes the following form:[18]

$$H_{\mathrm{CEF}}=\sum_{k}\sum_{q=-k}^{k} B_q^k C_q^k, \tag{4}$$

where the B_q^k denote the CEF parameters and the C_q^k are tensor operators of rank k. The point symmetry of the lattice site in question and the orbital angular momentum of the individual magnetic electrons limit the number of indices k and q. In particular, the presence of a center of inversion at the ion site cancels all the odd terms; a p-fold axis of rotation when chosen as polar axis reduces the Hamiltonian (4) to terms with $q=np$ (n integer). In addition, for the (in general) complex CEF parameters B_q^k the relation $B_{-q}^k=(-1^q)(B_q^k)^*$ holds. Thus, for the rare-earth nickelates with f electrons, orthorhombic symmetry (point group C_s at the R site) and the polar axis along the c direction, the CEF Hamiltonian involves terms with $k=2$, 4, 6, and even indices q, where all the off-diagonal CEF parameters ($q\neq 0$) are complex, giving rise to fifteen independent CEF parameters.

Usually the CEF potential is treated as a perturbation of the ground-state J multiplet $^{2S+1}L_J$ alone. For the presently studied compounds, however, this approximation cannot be applied, since the overall CEF splittings of the rare-earth nickelates are comparable in magnitude to the intermultiplet splittings. This leads to a mixing of the different J multiplets through the CEF interaction (J mixing). Furthermore, due to the spin-orbit coupling, S and L are no longer good quantum numbers. Indeed, every J multiplet is composed of terms with different L, S, but same J (intermediate coupling). In our calculations, we have addressed these effects in first order by including the electrostatic and spin-orbit interactions in the Hamiltonian:[18]

$$H=H_{\mathrm{el}}+H_{\mathrm{SO}}+H_{\mathrm{CEF}}, \tag{5}$$

where

$$H_{\mathrm{el}}+H_{\mathrm{SO}}=\sum_{k=2,4,6} F^k f_k+\xi A_{\mathrm{SO}}. \tag{6}$$

The adjustable free-ion parameters F^k and ξ correspond to Slater electrostatic and spin-orbit integrals, respectively; they have been taken from Ref. 19. A_{SO} and f_k represent matrix elements for the angular parts of the spin-orbit and electrostatic interactions, respectively, which have been tabulated by Nielson and Koster.[20] In order to avoid the diagonalization of excessively large matrices (rank 2002 in the case of Sm^{3+}) in the least-squares refinements, we used a common truncation scheme:[21] First, the free-ion Hamiltonian (6) was diagonalized separately for each J value for the given F^k and ξ. The eigenvectors derived from this diagonalization were then used to project the full Hamiltonian (5) to this new intermediate-coupling basis. In the final diagonalization, only levels in J multiplets below a certain energy were included. This cutoff energy was chosen such that changes in the final energies and transition matrix elements $\langle j|\mathbf{m}_p|i\rangle$ remained well below the experimental accuracy.

The number of observables resulting from neutron-spectroscopic CEF investigations is usually not sufficient to determine all the CEF parameters defining the Hamiltonian (4), thus some approximations have to be adopted. We can factorize each CEF parameter B_q^k into a structural and an electronic part:

$$B_q^k=\gamma_q^k\langle r^k\rangle A_q^k. \tag{7}$$

Here, A_q^k is a reduced CEF parameter describing the charge distribution surrounding the R ion, $\langle r^k\rangle$ is the k^{th} moment of the radial distribution of the $4f$ electrons, and

$$\gamma_q^k=(-1)^q\sqrt{\frac{4\pi}{2k+1}}\sum_j \frac{1}{R_j^{k+1}}Y_{-q}^k(\Theta_j,\Phi_j) \tag{8}$$

is a geometrical coordination factor as defined by Hutchings,[22] in which R_j denotes the distance of the jth coordinating ligand ion to the rare-earth ion and Y_q^k is a spherical harmonic. The sum in Eq. (8) is rapidly converging for $k=4$ and $k=6$, thus the fourth- and sixth-order CEF parameters are well defined by taking into account only the nearest-neighboring coordination shell in the calculation of the geometrical coordination factors γ_q^k. Moreover, as repeatedly shown in the past for several perovskite-type compounds,[14,15] the reduced CEF parameters A_q^k are essentially independent of k. We can therefore make use of the correlation

$$B_q^k=\frac{\gamma_q^k}{\gamma_0^k}B_0^k. \tag{9}$$

Furthermore, assuming that the electronic properties do not change when replacing a rare-earth $R1$ with another rare-earth $R2$, the CEF parameters for $R2$ can be extrapolated from the CEF parameters determined for $R1$ according to

$$B_q^k(R2)=\frac{\gamma_q^k(R2)}{\gamma_q^k(R1)}\frac{\langle r^k(R2)\rangle}{\langle r^k(R1)\rangle}B_q^k(R1). \tag{10}$$

The second-order terms of the CEF potential, on the other hand, have a long-range nature, so that Eq. (9) and Eq. (10) do not apply.

TABLE I. Structural parameters of $Pr_{1-x}La_xNiO_3$ determined from neutron powder diffraction at $T=1.5$ K, from Ref. 13. For *Pbnm* the Wyckoff positions are: *R*: 4c $(x,y,1/4)$; Ni: 4b (1/2,0,0); O1: 4c $(x,y,1/4)$; O2: 8d (x,y,z). For $R\bar{3}c$: *R*: 6a (0,0,1/4); Ni: 6b (0,0,0); O: 18e $(x,0,1/4)$. For each compound, the nearest-neighboring *R*-O distances $d_{R\text{-}O}$ and their multiplicity are also given. The errors quoted are statistical only.

$Pr_{1-x}La_xNiO_3$	$x=0.05$	$x=0.1$	$x=0.15$	$x=0.2$	$x=0.25$	$x=0.5$		$x=0.7$
Space group	*Pbnm*	*Pbnm*	*Pbnm*	*Pbnm*	*Pbnm*	*Pbnm*		$R\bar{3}c$
a (Å)	5.4171(1)	5.4202(1)	5.4256(1)	5.4273(1)	5.4310(1)	5.4513(1)		5.4486(2)
b (Å)	5.3823(1)	5.3815(1)	5.3828(1)	5.3800(1)	5.3756(1)	5.3760(1)		
c (Å)	7.6168(2)	7.6181(1)	7.6228(2)	7.6207(1)	7.6128(1)	7.6151(1)		13.0363(2)
R								
x	0.9945(5)	0.9951(4)	0.9954(4)	0.9957(3)	0.9960(3)	0.9975(3)		
y	0.0315(4)	0.0294(4)	0.0285(4)	0.0275(4)	0.0256(3)	0.0191(4)		
B (Å^2)	0.21(3)	0.24(3)	0.23(3)	0.18(3)	0.12(2)	0.36(2)		0.46(6)
Ni								
B (Å^2)	0.09(2)	0.05(2)	0.06(2)	0.05(2)	0.11(2)	0.30(2)		0.23(2)
O1								
x	0.0704(4)	0.0695(3)	0.0686(3)	0.0674(3)	0.0659(2)	0.0627(3)		0.5503(4)
y	0.4921(4)	0.4921(4)	0.4942(4)	0.4934(4)	0.4941(3)	0.4965(5)		
B (Å^2)	0.20(4)	0.18(4)	0.24(4)	0.18(3)	0.18(3)	0.46(3)		0.58(5)
O2								
x	0.7190(3)	0.7199(2)	0.7206(2)	0.7217(2)	0.7238(2)	0.7300(3)		
y	0.2817(2)	0.2812(2)	0.2806(2)	0.2794(2)	0.2770(2)	0.2715(3)		
z	0.0367(2)	0.0369(2)	0.0366(2)	0.0363(2)	0.0351(1)	0.0333(2)		
B (Å^2)	0.27(3)	0.19(3)	0.18(3)	0.20(2)	0.26(2)	0.43(2)		
d_{R-O1} (Å)								
$(\times 1)$	2.366(2)	2.369(2)	2.373(2)	2.378(2)	2.385(1)	2.401(1)	$(\times 3)$	2.450(1)
$(\times 1)$	2.513(2)	2.523(2)	2.538(2)	2.537(2)	2.547(2)	2.591(2)	$(\times 6)$	2.696(1)
$(\times 1)$	2.932(2)	2.919(2)	2.902(2)	2.900(1)	2.882(1)	2.832(2)	$(\times 3)$	2.998(3)
$(\times 1)$	3.067(2)	3.067(1)	3.065(1)	3.062(1)	3.056(1)	3.056(2)		
d_{R-O2} (Å)								
$(\times 2)$	2.405(2)	2.404(2)	2.408(2)	2.414(2)	2.427(1)	2.457(2)		
$(\times 2)$	2.585(2)	2.588(2)	2.590(2)	2.589(2)	2.586(1)	2.586(2)		
$(\times 2)$	2.694(2)	2.702(2)	2.706(2)	2.710(1)	2.714(1)	2.744(1)		
$(\times 2)$	3.165(1)	3.156(1)	3.149(1)	3.137(1)	3.110(1)	3.050(1)		
χ^2	0.68	0.60	0.51	0.56	0.59	1.96		13.04
R_{Bragg}	2.02	2.10	2.26	2.00	1.91	3.21		7.88

In the analysis of the present data, we have partially made use of Eq. (9) and Eq. (10) in order to keep the number of fitting parameters smaller than the number of observables (CEF energies and intensities) and to obtain good starting parameters for the fitting procedure. The structural parameters for the calculation of the geometrical coordination factors have been taken from Ref. 9 for $R=$ Eu and Sm, Ref. 12 for $R=$ Nd and Pr, and Ref. 13 for $R=Pr_{1-x}La_x$. The rel-

TABLE II. Geometrical constraints used in the determination of the CEF parameters in $RNiO_3$.

R	$\Re(B_2^4)/B_0^4$	$\Im(B_2^4)/B_0^4$	$\Re(B_4^4)/\Im(B_4^4)$	$\Re(B_2^6)/B_0^6$	$\Im(B_2^6)/B_0^6$	$\Im(B_4^6)/\Re(B_4^6)$	$\Re(B_6^6)/B_0^6$	$\Im(B_6^6)/B_0^6$
Eu	0.165	1.072	0.167	−0.272	0.536	−0.031	−0.238	−0.017
Sm	0.125	0.956	0.206	−0.248	0.534	−0.037	−0.266	−0.004
Nd	0.136	1.031	0.374	−0.213	0.523	−0.017	−0.296	−0.036
Pr	0.104	0.891	0.396	−0.207	0.497	0.004	−0.308	−0.011
$Pr_{0.95}La_{0.05}$	0.102	0.899	0.420	−0.205	0.491	0.014	−0.307	−0.014
$Pr_{0.90}La_{0.10}$	0.104	0.896	0.434	−0.207	0.491	0.018	−0.316	−0.014
$Pr_{0.85}La_{0.15}$	0.106	0.881	0.456	−0.214	0.493	0.015	−0.327	−0.007
$Pr_{0.80}La_{0.20}$	0.097	0.860	0.462	−0.205	0.486	0.018	−0.315	−0.004
$Pr_{0.75}La_{0.25}$	0.091	0.817	0.493	−0.200	0.471	0.020	−0.314	0.007
$Pr_{0.50}La_{0.50}$	0.089	0.720	0.607	−0.212	0.433	0.030	−0.343	0.036

TABLE III. CEF parameters (in meV) for RNiO$_3$ determined in the present work.

R	B_0^2	$\Re(B_2^2)$	$\Im(B_2^2)$	B_0^4	$\Im(B_4^4)$	B_0^6	$\Re(B_4^6)$
Eu	-23.4 ± 0.5	$-0.095\times\Im(B_2^2)$	-57.7 ± 0.8	-81.2	97.2	-76.2	-186.1
Sm	-8.7 ± 5.4	7.3 ± 3.9	-47.9 ± 2.4	-77.5 ± 1.5	$-1.11\times B_0^4$	-97.9 ± 7.7	-142.8 ± 7.6
Nd	-19.1 ± 3.4	18.8 ± 1.2	-80.3 ± 1.0	-100.4 ± 1.6	$-0.76\times B_0^4$	-94.6 ± 5.0	-164.5 ± 1.0
Pr	-8.3 ± 1.6	28.7 ± 1.0	-62.2 ± 0.4	-98.8 ± 2.4	46.9 ± 3.0	-61.6 ± 6.0	-183.7 ± 1.4
$Pr_{0.95}La_{0.05}$	-8.2 ± 2.0	29.0 ± 2.0	-62.3 ± 1.2	-100.1 ± 1.4	46.6 ± 5.6	-60.3 ± 7.3	-186.0 ± 2.7
$Pr_{0.90}La_{0.10}$	-7.3 ± 4.5	29.5 ± 1.8	-60.5 ± 1.5	-98.8 ± 2.8	46.7 ± 6.0	-65.8 ± 8.3	-184.9 ± 5.7
$Pr_{0.85}La_{0.15}$	-6.6 ± 5.0	30.1 ± 2.0	-59.2 ± 1.6	-98.2 ± 2.6	47.9 ± 6.5	-69.3 ± 7.4	-185.3 ± 6.2
$Pr_{0.80}La_{0.20}$	-4.6 ± 4.7	29.9 ± 2.0	-58.1 ± 1.6	-98.9 ± 2.8	48.0 ± 6.4	-72.2 ± 8.3	-185.9 ± 6.0
$Pr_{0.75}La_{0.25}$	0.9 ± 4.8	31.6 ± 2.2	-53.2 ± 2.3	-98.8 ± 3.1	50.4 ± 7.3	-80.4 ± 7.9	-185.2 ± 7.0
$Pr_{0.50}La_{0.50}$	27.2 ± 3.4	38.9 ± 2.0	-39.6 ± 3.7	-104.1 ± 2.5	48.2 ± 5.4	-68.6 ± 8.0	-192.3 ± 8.1

evant structural parameters for the latter are listed in Table I. The geometrical constraints utilized in the data analysis are listed in Table II.

III. RESULTS AND DATA ANALYSIS

A. $EuNiO_3$

The lowest-lying J multiplets of the free Eu^{3+} ion are the singlet and triplet states $^7F_0$ and $^7F_1$. Thus, there is no CEF splitting in the ground-state J multiplet, and the CEF potential of the first-excited J multiplet is restricted to second-order terms in the Hamiltonian (4). This gives the unique opportunity to determine experimentally the long-range part of the CEF potential in the rare-earth nickelates, which is difficult to estimate by any model calculation.

The experimental data and analysis for this compound have already been published elsewhere[23] and we only give a brief summary of the results. In the experiments carried out on the time-of-flight spectrometer LRMECS, all three intermultipet transitions from the ground state $^7F_0$ to the CEF split first-excited multiplet $^7F_1$ were observed at energies $A=34.5$, $B=43.8$, and $C=60.9$ meV, respectively. For the data analysis there are four adjustable parameters, the three CEF parameters B_0^2, $\Re(B_2^2)$, and $\Im(B_2^2)$, as well as the spin-orbit parameter ξ. A fit to the three observed energies alone requires a constraint in the number of adjustable parameters, thus the smallest CEF parameter, $\Re(B_2^2)$, was geometrically correlated to $\Im(B_2^2)$. The best fitted parameters are listed in Table III. The spin-orbit parameter ξ, listed in Table IV, turned out to be smaller by 1.5% than for the standard (R:LaF_3, Ref. 19) used in the remainder of the present work. The reliability of the CEF parameters was checked by comparing the observed and calculated intensities of the CEF split multiplet transitions according to the cross-section formula (3). As shown in Ref. 23, the agreement is excellent.

TABLE IV. Free-ion electrostatic F^k and spin-orbit ξ parameters (in meV) from Ref. 19 used in the calculation of the CEF interaction in RNiO$_3$. For $R=$Eu and Sm, the values of ξ derived in this work are given. N_J denotes the number of J multiplets included in the calculation as described in Sec. II C.

R	F^2	F^4	F^6	ξ	N_J
Eu	10306	7348	5276	163.3 ± 0.5	15
Sm	9895	7089	4990	145.5 ± 0.4	12
Nd	9053	6545	4433	109.8	4
$Pr_{1-x}La_x$	8540	6242	4079	93.2	6

Although the fourth- and sixth-order CEF parameters could not be derived from the spectroscopic data, they have some influence on the low-lying electronic states through the admixture of higher J multiplets. This was taken into account in the calculations using the corresponding CEF parameters of the isostructural compound $NdGaO_3$,[24,25] extrapolating to $EuNiO_3$ according to Eq. (10), thereby obtaining the values listed in Table III.

B. $PrNiO_3$

The CEF interaction in $PrNiO_3$ gives rise to a complete lifting of the degeneracy of the ground-state J-multiplet $^3H_4$ as shown in Fig. 2. Energy spectra obtained for $PrNiO_3$ with use of the triple-axis spectrometer MARC as well as the time-of-flight spectrometer MARI are shown in Fig. 3. There is evidence for five inelastic lines $A-E$ at 6.4, 15.0, 20.3,

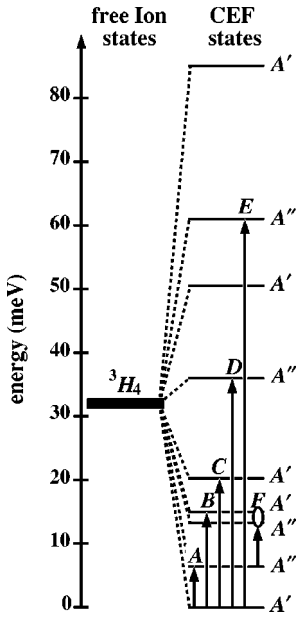

FIG. 2. CEF states of Pr^{3+} in $PrNiO_3$. The arrows denote the observed CEF transitions. The symmetry of the CEF states is given in the notation of J. L. Prather, Nat. Bur. Stand. Monograph 19, 1961.

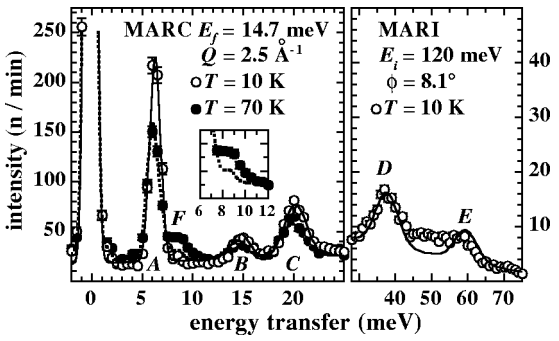

FIG. 3. Energy spectra of $PrNiO_3$. The lines denote calculated spectra for $T=10$ K (solid line) and $T=70$ K (dashed line) using the CEF parameters given in Table III, convoluted with the instrumental resolution function. The inset shows the observed and calculated intensity around transition F at $T=70$ K.

38, and 60 meV, respectively. The origin of these excitations can be derived from the dependence of their intensity on momentum transfer Q (shown in Fig. 4) and temperature. According to the cross-section formula (3), the Q dependence was modeled as

$$I(Q)=I_m f_{\mathrm{Pr}}^2(Q)e^{-2W_m}+I_p Q^2 e^{-2W_p}+I_{\mathrm{mScat}}, \qquad (11)$$

where I_m, I_p, and I_{mScat} denote the magnetic, phononic, and the Q-independent contribution from multiple scattering, respectively. The Debye-Waller factors W_x were described in terms of the isotropic temperature factors B_x as $W_x=B_x(Q/4\pi)^2$. For the least-squares fitting of Eq. (11) to the data shown in Fig. 4, the isotropic temperature factor for the magnetic contribution was held fixed at the value $B_m=B_{\mathrm{Pr}}$ obtained from Rietveld refinements to neutron powder diffraction data.[12] The values for B_p obtained from the best fits to Eq. (11) are in agreement with the phononic contribution to the transitions $A-C$ (D,E) arising mainly from Pr and Ni (O) modes. From this analysis, shown in Fig. 4, we conclude that at small momentum transfer Q all excitations $A-E$ are of magnetic origin. The observed decrease in intensity with increasing temperature (see Fig. 3) then unambiguously attributes these excitations to ground-state CEF transitions, as depicted in Fig. 2.

For the data analysis we have therefore nine observables, namely five energies and four intensity ratios of different

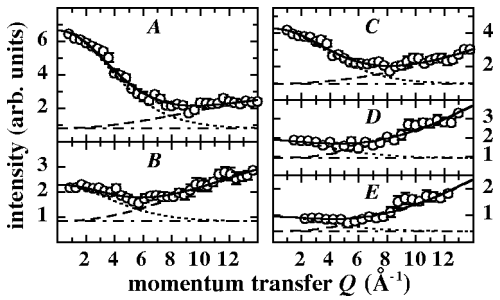

FIG. 4. Q dependence of the transitions $A-E$ in $PrNiO_3$ measured on MARI with an incident energy $E_i=120$ meV at $T=10$ K. The solid lines are the results from least squares fits to Eq. (11), consisting of a magnetic (dotted line), a phononic (dashed line), and a constant contribution arising from multiple scattering (dash-dotted line).

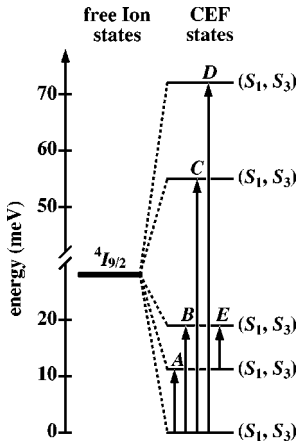

FIG. 5. CEF states of Nd^{3+} in $NdNiO_3$. Symbols are as in Fig. 2. The states (S_1, S_3) are Kramers-conjugate states.

CEF transitions. This is clearly not sufficient to determine the 15 CEF parameters, and some restrictions or correlations have to be introduced in order to arrive at a reliable set of starting parameters for the least-squares fitting procedure. First, for the second-order CEF parameters we have taken the values obtained for $EuNiO_3$ (see Sec. III A). Second, for the fourth- and sixth-order terms we extrapolated the CEF parameters determined for $NdGaO_3$ (Refs. 24,25) to $PrNiO_3$ according to Eq. (10) by including the eight nearest-neighbor oxygen ions for the calculation of the geometry factors γ_q^k. Using these CEF parameters already gave a reasonable description of the observed energy spectra displayed in Fig. 3. We then examined in detail the influence of each CEF parameter on the energy spectra and found B_0^4, $\Im(B_4^4)$, B_0^6, and $\Re(B_4^6)$ to be the leading CEF parameters for $PrNiO_3$. In the least-squares fitting procedures consequently all the leading as well as all the second-order CEF parameters were allowed to vary independently, whereas the remaining CEF parameters were correlated according to Eq. (9) as listed in Table II. The results as listed in Table III reproduce the observed energy spectra fairly well (see Fig. 3) both for $T=10$ and 70 K. The discrepancy between the observed and calculated intensity at 70 K for the transition F, corresponding to the excited transitions from the second to the third and fourth level as depicted in Fig. 2, is probably due to a Van Hove singularity in the phonon density of states. Although the phonon dispersions in the $RNiO_3$ compounds have not been determined because single crystals are not available, the isostructural $NdGaO_3$ indeed shows three almost dispersionless branches in this energy region.[26]

C. $NdNiO_3$

The CEF interaction in $NdNiO_3$ splits the tenfold degeneracy of the ground-state J-multiplet $^4I_{9/2}$ into five Kramers doublets as illustrated in Fig. 5. Energy spectra observed for $NdNiO_3$ with use of the triple-axis spectrometer MARC are shown in Fig. 6. Four ground-state CEF transitions $A-D$ show up at energies of 11.2, 19.0, 66, and 72 meV, respectively, thus the CEF splitting pattern is completely determined. In addition, at higher temperatures we have observed an additional line at around 8 meV, corresponding to a transition between the first- and second-excited CEF state.

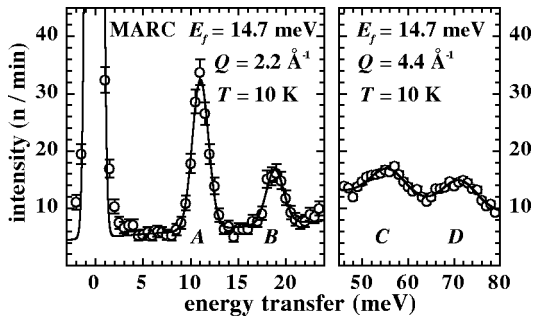

FIG. 6. Energy spectra of $NdNiO_3$ measured on MARC with fixed final energy $E_f = 14.7$ meV at $T = 10$ K. Lines are as in Fig. 3.

Again, the number of observables (four energies and four intensity ratios) was not sufficient to determine all the disposable CEF parameters independently, thus we proceeded in the least-squares refinement as outlined in Sec. III B. Furthermore, the variation of B_4^4 had only a negligible influence on the energy spectra and was therefore correlated to B_0^4 according to Eq. (9). The resulting CEF parameters, listed in Table III, provide an excellent description of the observed energy spectra, as is seen in Fig. 6.

D. $SmNiO_3$

The lowest-lying J multiplets of the free Sm^{3+} ion are the states $^6H_{5/2}$ and $^6H_{7/2}$ which are split by the CEF interaction in $SmNiO_3$ into three and four Kramers doublets, respectively, as illustrated in Fig. 7. Figure 8 shows the energy spectra observed for $SmNiO_3$ with use of the time-of-flight spectrometers HET and MARI. Within the ground-state J multiplet there are two weak CEF excitations A and B at 19 and 35 meV, respectively, superimposed on a phonon background. Four ground-state CEF transitions $C-F$ into the first-excited J multiplet show up at 132, 142, 160, and 179 meV, respectively. For the least-squares fit we used the same procedure as outlined in Sec. III C. The starting values of the

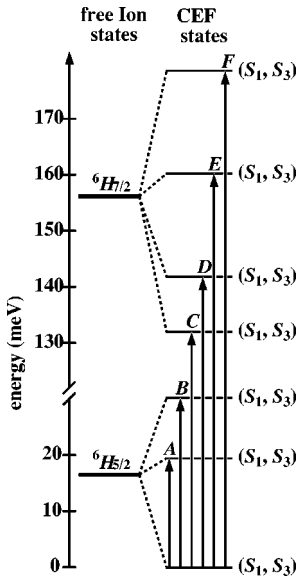

FIG. 7. CEF states of Sm^{3+} in $SmNiO_3$. Symbols are as in Fig. 2. The states (S_1, S_3) are Kramers-conjugate states.

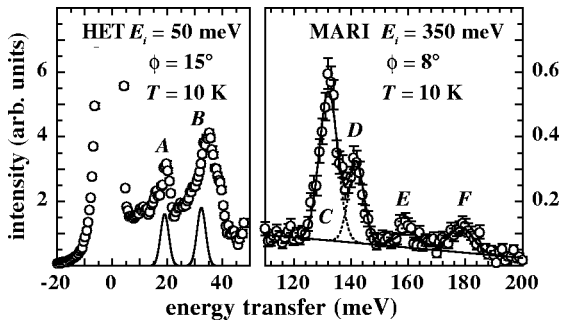

FIG. 8. Energy spectra of $SmNiO_3$ at $T = 10$ K. Lines are as in Fig. 3.

CEF parameters gave already a very good description of the observed energy spectra. In the fitting procedure the CEF parameters converged to the values listed in Table III. The spin-orbit parameter ξ was also allowed to vary, however, in contrast to $EuNiO_3$, the fitted value listed in Table IV agrees very well with the standard value for $Sm:LaF_3$.[19] The agreement between observed and calculated energies and intensities is excellent for the excited J multiplet, whereas a detailed comparison for the intensities of the ground-state J multiplet is made difficult because of the weakness of the CEF transitions compared to the phonon scattering in the energy range of interest.

E. $Pr_{1-x}La_xNiO_3$

The study of the CEF interaction in the mixed compounds $Pr_{1-x}La_xNiO_3$ is of particular interest. Firstly, we can tune the metal-insulator transition in the temperature range 130 K$\geq T_{MI} \geq$0 K upon variation of the La content up to $x = 0.25$ and thereby investigate localization effects of the electrons. Secondly, while the compound has orthorhombic symmetry $Pbnm$ for $x < 0.7$, the system crystallizes in the rhombohedral symmetry $R3c$ for $x \geq 0.7$. For rhombohedral symmetry, the degeneracy of the ground-state J multiplet is no longer completely lifted, but splits up into three singlet and three doublet CEF states. The CEF ground state may

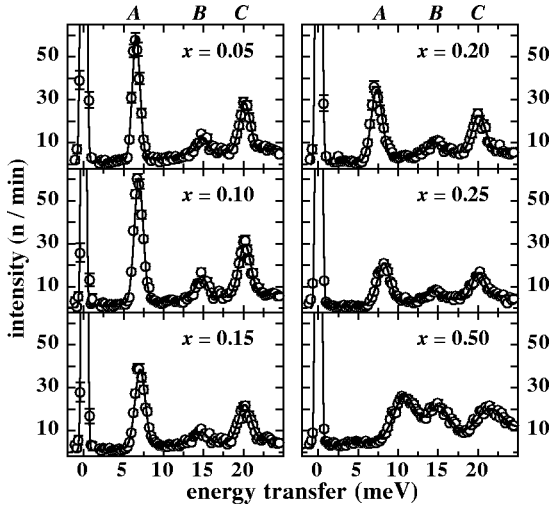

FIG. 9. Energy spectra of $Pr_{1-x}La_xNiO_3$ measured on IN3 with $E_f = 13.7$ meV at $Q = 2.5$ Å^{-1} and $T = 10$ K. Lines are as in Fig. 3.

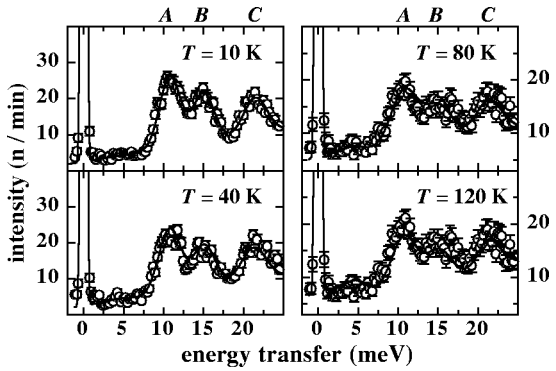

FIG. 10. Energy spectra of $Pr_{0.5}La_{0.5}NiO_3$ measured on IN3 with $E_f = 13.7$ meV at $Q = 2.5$ Å^{-1}. Lines are as in Fig. 3.

therefore be a doublet with basically different properties compared to a singlet ground state.

Figure 9 shows the low-energy part of the spectra observed for orthorhombic $Pr_{1-x}La_xNiO_3$ ($0.05 \leqslant x \leqslant 0.50$) with use of the triple-axis spectrometer IN3. The ground-state CEF transitions *A*, *B*, and *C* exhibit a different behavior upon variation of the La content *x*. The energy of the line *A* moves continuously to higher energies with increasing *x*, whereas its intensity is decreasing. The energies of the lines *B* and *C* appear to be unaffected by *x*, but their intensities change oppositely to each other. For all three CEF transitions we observe a broadening of the linewidths with increasing *x*, which is most likely due to enhanced local structural inhomogeneities around the Pr^{3+} ions. All the above-mentioned changes are also continuous at the transition from the insulating ($x \leqslant 0.20$) to the metallic ($x \geqslant 0.25$) state, i.e., the CEF interaction does not show any abrupt response to the electronic delocalization.

Since the changes of the observed energy spectra are continuous, we can perform the least-squares fitting procedure also in a continuous manner along the series with increasing La content. The resulting CEF parameters as listed in Table III provide an excellent description of the observations, see Fig. 9. It is important to note that the increased substitution of Pr by La has little effect on the higher excited CEF transitions *D* and *E* (see Sec. III B) for which no experimental data are available. However, the reliability of the CEF parameters can be checked by studying the temperature dependence of the CEF spectra. This is shown in Fig. 10 for $x = 0.50$. Again, the agreement between the observed and calculated energy spectra is rather good. Furthermore, as Fig. 11 shows, the CEF parameters vary smoothly but systematically with *x* as expected.

Figure 12 shows energy spectra observed for rhombohedral $Pr_{0.3}La_{0.7}NiO_3$ with use of the triple-axis spectrometer IN3. The data are considerably different from the orthorhombic analogs displayed in Fig. 9, and they have to be analyzed on the basis of the CEF Hamiltonian for rhombohedral symmetry:

$$H_{\mathrm{CEF}} = B_0^2 C_0^2 + B_0^4 C_0^4 + B_3^4 (C_3^4 - C_{-3}^4) + B_0^6 C_0^6 + B_3^6 (C_3^6 - C_{-3}^6) + B_6^6 (C_6^6 + C_{-6}^6), \qquad (12)$$

where now all the CEF parameters are real quantities. Without any further considerations, a reliable parametrization of the data would be extremely difficult. We therefore proceeded in the following way. First, we calculated the reduced CEF parameters A_q^k for the pure Pr-compound according to Eq. (7). Using these reduced CEF parameters and the structural parameters given in Table I for $R = Pr_{1-x}La_xNiO_3$ and in Ref. 9 and 12 for $R =$ Eu, Sm, Nd, and Pr, we then calculated, according to Eq. (10), the variation of the CEF parameters across the rare-earth series expected from structural changes alone (dotted lines in Fig. 11). For $R =$ Nd, Sm, and Eu, the structural effects explain the variation of the CEF parameters fairly well. However, this is not the case across the $R = Pr_{1-x}La_x$ series. This means that for an extrapolation of the CEF parameters from the orthorhombic to the rhombohedral structure, electronic effects have to be taken into

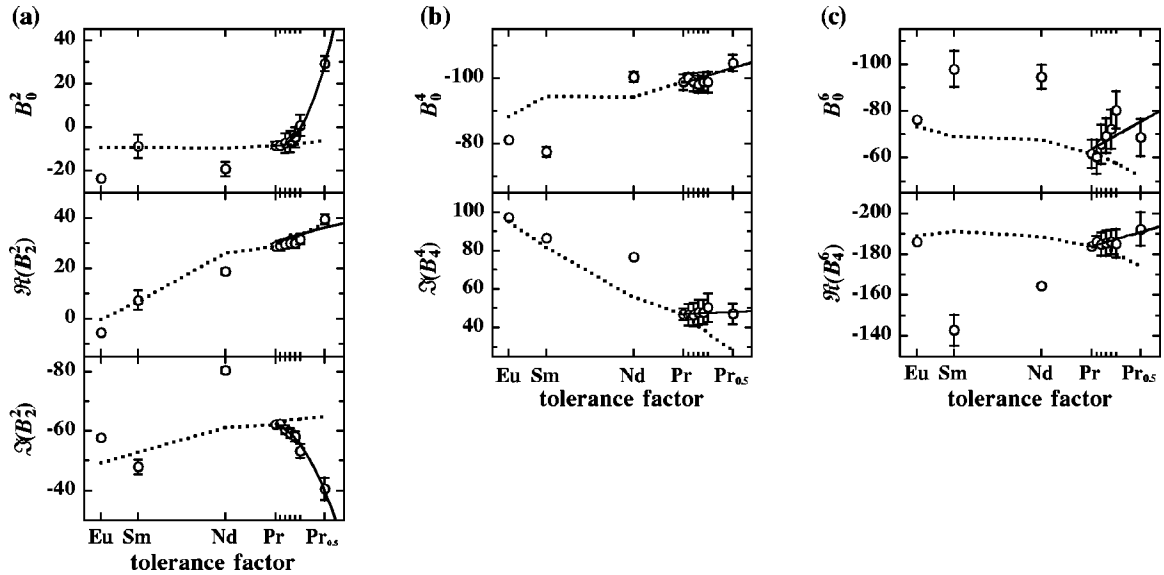

FIG. 11. Variation of the CEF parameters as a function of the tolerance-factor *t*. The dotted lines denote the variation expected from structural changes alone. The solid lines denote the empirical laws used to extrapolate the CEF parameters from the orthorhombic to the rhombohedral structure as explained in Sec. III E.

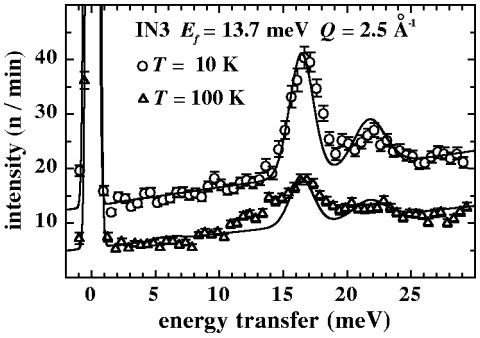

FIG. 12. Energy spectra of rhombohedral $Pr_{0.3}La_{0.7}NiO_3$ measured on IN3 with $E_f = 13.7$ meV. Lines are as in Fig. 3.

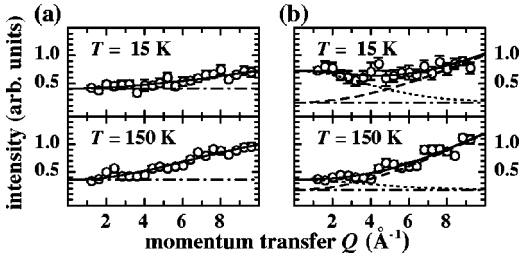

FIG. 13. Q dependence of the scattering intensity in $Pr_{0.3}La_{0.7}NiO_3$ measured on MARI with an incident energy $E_i = 60$ meV, integrated over the energy transfer range (a) $\hbar\omega = 14 \pm 1$ and (b) $\hbar\omega = 16.5 \pm 1$ meV (transition A). Lines are as in Fig. 4.

account as well. However, because the electronic effects manifest themselves differently for different CEF parameters (see Fig. 11), we used empirical quadratic ($k=2$) and linear ($k=4,6$) laws for the variation of the reduced CEF parameters $A_q^k(x)$, which, together with the structural variation, leads to the CEF parameters $B_q^k(x)$ shown as solid lines in Fig. 11. The CEF potential of rhombohedral symmetry with the polar axis along the [111] direction furthermore requires to be expressed by a rotation $R(\alpha,\beta,\gamma)$ of the orthorhombic frame of reference with the polar axis along [001], where the Euler angles are $\alpha = 60°$, $\cos\beta = \sqrt{3}/3$, and $\gamma = 90°$. The CEF parameters $B_q^k(r)$ of the rhombohedral state are then related to the CEF parameters $B_q^k(o)$ in the orthorhombic state by[27]

$$B_q^k(r) = \sum_{q'} B_{q'}^k(o) D_{qq'}^k, \tag{13a}$$

where $D_{mm'}^j$ is defined by:

$$R(\alpha,\beta,\gamma)|jm\rangle = \sum_{m'} D_{m'm}^j(\alpha,\beta,\gamma)|jm'\rangle. \tag{13b}$$

Another problem is the number of oxygen ions that have to be included in the nearest-neighboring coordination shell of rhombohedral $Pr_{1-x}La_xNiO_3$, which may be either nine or twelve. As the calculations yield only minor differences between the two cases, we used throughout a nearest-neighboring coordination shell comprising twelve oxygen ions. The extrapolation described above predicts the CEF ground state to be a doublet, followed by excited CEF states between 15 and 30 meV and a high lying CEF state at 60 meV, in reasonable agreement with the energy spectra shown in Fig. 12. In the least-squares fitting procedure all the diagonal CEF parameters were allowed to vary independently, whereas the remaining CEF parameters were correlated according to Eq. (9). The best fit was obtained for

$B_0^2 = 20 \pm 3$ meV $\quad B_0^4 = 34 \pm 3$ meV $\quad B_0^6 = -139 \pm 4$ meV
$B_3^4 = -1.09 B_0^4 \quad B_3^6 = 0.49 B_0^6 \quad B_6^6 = 7.73 B_0^6$.

As Fig. 12 shows, these CEF parameters provide a reasonably good description of the observed energy spectra at low temperatures, but as in the case of the orthorhombic compounds, there is again additional intensity at higher temperatures. However, the Q dependence of this additional scattering, shown in Fig. 13 together with the Q dependence of transition A, clearly indicates that this intensity is due to phononic rather than magnetic scattering.

The CEF splitting patterns of the mixed compounds $Pr_{1-x}La_xNiO_3$ are summarized in Fig. 14. The zero point in the energy scale corresponds to the weighted average of all the CEF levels in the ground-state J-multiplet $^3H_4$. The most crucial conclusion from our investigation concerns the nature of the electronic ground state, which changes from a singlet to a doublet state at the orthorhombic-to-rhombohedral phase transition. Accordingly, the thermodynamic properties are expected to be drastically different in the two crystallographic states as discussed below.

IV. DISCUSSION

Because of the low symmetry at the rare-earth site in $RNiO_3$, the CEF interaction contains many parameters, which make an unambiguous determination difficult. In the present case, we made use of geometrical constraints to reduce the number of free parameters. A check of the reliability of the parameters can be obtained by examining the behavior as a function of the rare-earth, and by comparison of calculated thermodynamic properties with experiments. As is seen from Fig. 11, the CEF parameters determined in this

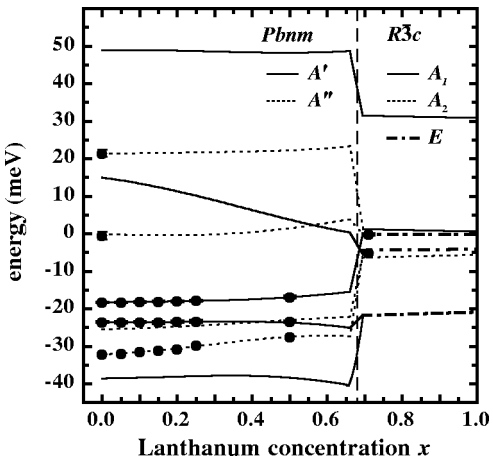

FIG. 14. CEF energy level schemes of the Pr^{3+} ions in $Pr_{1-x}La_xNiO_3$. The data points denote the observed energy levels. The symmetry notation is as in Fig. 2.

work vary smoothly over all the compounds studied. There are discontinuities in the B_q^6 parameters for $R=$ Sm and Nd, which mainly arise because for these compounds B_4^4 was correlated to B_0^4, whereas it was freely varied for the Pr compounds. Furthermore, the calculated saturation moment $\mu_{\mathrm{Nd}}=1.75$ and $\mu_{\mathrm{Sm}}=0.3\ \mu_B$ are in excellent agreement with the values $\mu_{\mathrm{Nd}}=2.0(2)$ and $\mu_{\mathrm{Sm}}=0.3(1)\ \mu_B$ obtained from neutron-diffraction studies of the magnetic ordering.[8,9] We therefore conclude that we have determined reliable CEF parameters for all $R\mathrm{NiO_3}$ compounds investigated.

Although first synthesized almost thirty years ago,[28] it wasn't until the renewed investigations following the discovery of high-temperature superconductivity that the metal-insulator transition in the rare-earth nickelates was revealed.[2] The driving mechanism of the transition is, however, not yet fully elucidated. Torrance *et al.*[7] first suggested that the electronic localization is due to the closing of the Ni-O-Ni superexchange angle by thermal contraction, which would reduce the Ni_{3d}-O_{2p} orbital overlap beyond a critical value, and thereby produce the gap opening. Since the Ni-O-Ni angle at a given temperature decreases with decreasing rare-earth ionic size, this picture would also explain the increase of T_{MI}, and hence the semiconducting gap, along the rare-earth series. More recently, the scenario has changed somewhat after the observation of large ^{18}O-^{16}O isotope shifts in the MI transition temperatures of the first members of the series ($R=$ Pr, Nd, Sm, Eu),[6] and a $2\mathrm{Ni}^{3+}\rightarrow\mathrm{Ni}^{3+\alpha}+\mathrm{Ni}^{3-\alpha}$ ($\alpha\approx0.35$) charge disproportionation at the gap opening in the heavy rare-earth nickelate $\mathrm{YNiO_3}$.[29] Though these results clearly establish the importance of the electron-lattice coupling as driving force for the MI transition, they are not in contradiction with the decrease of the Ni_{3d}-O_{2p} hybridization along the series inferred from previous structural studies.

As already noted in Sec. III E and shown in Fig. 11, the CEF parameters show an increasing departure from the variation expected if changes were controlled by structural effects only. This indicates an increasing change of the local charge distribution surrounding the rare-earth ion towards the insulator-metal transition, possibly due to the increasing Ni_{3d}-O_{2p} hybridization. In an attempt to quantify these changes, we make use of an effective point charge model, in which the reduced CEF parameters in Eq. (7) are directly proportional to the charges at the nearest oxygen neighbors. Choosing an arbitrary fixpoint for A_q^k at $R=$ Pr, i.e.,

$$A_q^k(R)=A_q^k(Pr)[1-\delta_q^k(R)], \tag{14}$$

the change in the effective oxygen charges over the rare-earth series is obtained from the observed CEF parameters, the knowledge of the structural parameters, and Eq. (7), Eq. (10), and Eq. (14) as

$$\delta_q^k(R)=1-\frac{B_q^k(R)}{B_q^k(Pr)}\frac{\gamma_q^k(Pr)}{\gamma_q^k(R)}\frac{\langle r^k(Pr)\rangle}{\langle r^k(R)\rangle}. \tag{15}$$

Figure 15 shows the average change of the effective oxygen charge obtained from the freely varied fourth- and sixth-order CEF parameters. This analysis yields an increase in the effective oxygen charge towards the insulator-metal transition, in contrast to an increase of the Ni_{3d}-O_{2p} hybridization inferred from the variation of the Ni-O-Ni superexchange angle. This discrepancy is, however, most likely due to the shortcoming of the point charge model in strongly covalent compounds such as the nickelates.[30,31]

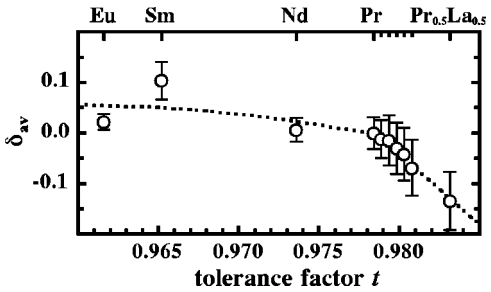

FIG. 15. Average relative change of the effective oxygen point charge obtained from the freely varied fourth- and sixth-order CEF parameters. The line is a guide to the eye.

An important conclusion from our experiments is the observation of a change of the Pr^{3+} ground-state symmetry across the structural phase transition in $\mathrm{Pr}_{1-x}\mathrm{La}_x\mathrm{NiO_3}$, which has a profound influence on the thermodynamic properties. The latter are related to the partition function Z, which is easily calculated from the known CEF level structure E_i:

$$Z=\sum_i e^{-E_i/k_BT}. \tag{16}$$

In particular, we predict a change in the entropy $\Delta S\approx5$ J/(mole K) between the rhombohedral ($x=0.7$) and the orthorhombic ($x=0.5$) phase of $\mathrm{Pr}_{1-x}\mathrm{La}_x\mathrm{NiO_3}$ at $T=10$ K. Since the structural transition occurs also as a function of external pressure and temperature,[5,32] the accompanying change in entropy gives way for a cooling principle by adiabatic pressure application, as was recently demonstrated by Müller *et al.*[33] Because of the strong dilution, long-range magnetic ordering induced by Pr-Pr exchange interactions is not expected to occur in the rhombohedral structure and so far, no sign of magnetic ordering has been observed down to 1.5 K. Nevertheless, the ground-state doublet in the rhombohedral structure will eventually be split at low temperatures either because of Pr^{3+} dimer or hyperfine interactions. The strengths of these interactions are currently unknown and subject of further investigations since they determine the low-temperature limit for the cooling mechanism. At present, however, we expect an entropy difference between the orthorhombic and rhombohedral phase, and therefore the possibility of cooling, down to the order of 100 mK.

In conclusion, we have investigated the crystal-field interaction in the $R\mathrm{NiO_3}$ compounds ($R=$ Eu, Sm, Nd, and $\mathrm{Pr}_{1-x}\mathrm{La}_x$, $x=0$, 0.05, 0.1, 0.15, 0.2, 0.25, 0.5, 0.7) by inelastic neutron scattering. Using geometrical constraints, we were able to determine the CEF parameters despite the low symmetry. The CEF parameters vary smoothly over all the compounds investigated and give a good agreement of the calculated magnetic properties with neutron powder diffraction investigations for $R=$ Sm and Nd. The variation of the CEF parameters towards and across the insulator-metal transition indicates an increasing change of the local charge dis-

tribution surrounding the rare-earth ion. However, an attempt to quantify a possible charge transfer failed because of the strong covalancy in these compounds. Across the structural phase transition at $x=0.7$, we found a change in the ground-state symmetry, which has pronounced effects on the thermodynamic properties, and opens the way for a new cooling technique by adiabatic pressure application.

ACKNOWLEDGMENTS

This work was financially supported by the Swiss National Science Foundation and the U.S. Department of Energy, Basic Energy Sciences, Division of Materials Science, under Contract No. W-31-109-ENG-38. Stimulating discussions with K. A. Müller are gratefully acknowledged.

*Present address: Materials Science Division, Argonne National Laboratory, Argonne IL 60439.

[1] J. B. Goodenough and P. M. Raccah, J. Appl. Phys. **36**, 1031 (1965).
[2] P. Lacorre, J. B. Torrance, J. Pannetier, A. I. Nazzal, P. W. Wang, and T. C. Huang, J. Solid State Chem. **91**, 225 (1991).
[3] P. C. Canfield, J. D. Thompson, S. W. Cheong, and L. W. Rupp, Phys. Rev. B **47**, 12 357 (1993).
[4] X. Obradors, L. M. Paulius, M. B. Maple, J. B. Torrance, A. I. Nazzal, J. Fontcuberta, and X. Granados, Phys. Rev. B **47**, 12 353 (1993).
[5] M. Medarde, J. Mesot, P. Lacorre, S. Rosenkranz, P. Fischer, and K. Gobrecht, Phys. Rev. B **52**, 9248 (1995).
[6] M. Medarde, P. Lacorre, K. Conder, F. Fauth, and A. Furrer, Phys. Rev. Lett. **80**, 2397 (1998).
[7] J. B. Torrance, P. Lacorre, A. I. Nazzal, E. J. Ansaldo, and Ch. Niedermayer, Phys. Rev. B **45**, 8209 (1992).
[8] J. L. García-Muñoz, J. Rodríguez-Carvajal, and P. Lacorre, Phys. Rev. B **50**, 978 (1994).
[9] J. Rodríguez-Carvajal, S. Rosenkranz, M. Medarde, P. Lacorre, M. T. Fernández-Díaz, F. Fauth, and V. Trounov, Phys. Rev. B **57**, 456 (1998).
[10] T. C. Huang, W. Parrish, H. Toraya, P. Laccore, and J. B. Torrance, Mater. Res. Bull. **25**, 1091 (1990).
[11] H. Obayashi and T. Kudo, Jpn. J. Appl. Phys. **14**, 330 (1975).
[12] J. L. García-Muñoz, J. Rodríguez-Carvajal, P. Lacorre, and J. B. Torrance, Phys. Rev. B **46**, 4414 (1992).
[13] S. Rosenkranz, Ph.D. thesis No. 11853, ETH Zürich, 1996.
[14] J. Mesot, P. Allenspach, U. Staub, A. Furrer, H. Mutka, R. Osborn, and A. D. Taylor, Phys. Rev. B **47**, 6027 (1993).
[15] U. Staub, J. Mesot, M. Guillaume, P. Allenspach, A. Furrer, H. Mutka, Z. Bowden, and A. D. Taylor, Phys. Rev. B **50**, 4068 (1994).
[16] M. L. Medarde, J. Phys.: Condens. Matter **9**, 1679 (1997).
[17] G. T. Trammell, Phys. Rev. **92**, 1387 (1953).
[18] B. G. Wybourne, *Spectroscopic Properties of Rare Earths* (Interscience, New York, 1965).
[19] W. T. Carnall, G. L. Goodman, K. Rajnak, and R. S. Rana, J. Chem. Phys. **90**, 3443 (1989).
[20] C. W. Nielson and G. F. Koster, *Spectroscopic Coefficients for the p^n, d^n, and f^n Configurations* (M.I.T., Cambridge, MA, 1964).
[21] W. T. Carnall, H. Crosswhite, H. M. Crosswhite, and J. G. Conway, J. Chem. Phys. **64**, 3582 (1976).
[22] M. T. Hutchings, in *Solid State Physics*, edited by F. Seitz and D. Turnbull (Academic, New York, 1964), Vol. 16, pp. 227.
[23] S. Rosenkranz, U. Staub, A. Furrer, R. Osborn, P. Lacorre, and V. Trounov, J. Alloys Compd. **250**, 577 (1997).
[24] A. Podlesnyak, S. Rosenkranz, F. Fauth, W. Marti, A. Furrer, A. Mirmelstein, and H. J. Scheel, J. Phys.: Condens. Matter **5**, 8973 (1993).
[25] W. Marti, M. Medarde, S. Rosenkranz, P. Fischer, A. Furrer, and C. Klemenz, Phys. Rev. B **52**, 4275 (1995).
[26] W. Marti, Ph.D. Thesis No 11158, ETH Zürich, 1995.
[27] A. R. Edmonds, *Angular Momentum in Quantum Mechanics* (Princeton University Press, Princeton, New Jersey, 1960).
[28] G. Demazeau, A. Marbeuf, M. Pouchard, and P. Hagenmüller, J. Solid State Chem. **3**, 582 (1971).
[29] J. A. Alonso, J. L. García-Muñoz, M. T. Fernández-Díaz, M. A. G. Aranda, M. J. Martínez-Lope, and M. T. Casais, Phys. Rev. Lett. **82**, 3871 (1999).
[30] M. Medarde, A. Fontaine, J. L. García-Muñoz, J. Rodríguez-Carvajal, M. d. Santis, M. Sacchi, G. Rossi, and P. Lacorre, Phys. Rev. B **46**, 14 975 (1992).
[31] T. Mizokawa, A. Fujimori, T. Arima, Y. Tokura, N. Mori, and J. Akimitsu, Phys. Rev. B **52**, 13 865 (1995).
[32] M. Medarde, J. Mesot, S. Rosenkranz, P. Lacorre, W. Marshall, S. Klotz, J. S. Loveday, G. Hamel, S. Hull, and P. Radaelli, Physica B **234-236**, 15 (1997).
[33] K. A. Müller, F. Fauth, S. Fischer, M. Koch, A. Furrer, and P. Lacorre, Appl. Phys. Lett. **73**, 1056 (1998).